POLITECNICO DI TORINO
Repository ISTITUZIONALE

Sustainable solid-state polymer electrolyte based on PEO-Xanthan gum blend for enhanced lithium-metal batteries

*Original*
Sustainable solid-state polymer electrolyte based on PEO-Xanthan gum blend for enhanced lithium-metal batteries / Patriarchi, A., Darjazi, H., Barcaioni, M., Minnetti, L., Fina, A., Filippov, A., Shah, F.U., Antzutkin, O.N., Muñoz-Márquez, M.Á., Nobili, F.. - In: JOURNAL OF POWER SOURCES. - ISSN 0378-7753. - STAMPA. - 663:(2026), pp. 1-12. [10.1016/j.jpowsour.2025.238856]

*Availability:*
This version is available at: 11583/3017225 since: 2026-10-30T09:12:46Z

*Publisher:*
Elsevier

*Published*
DOI:10.1016/j.jpowsour.2025.238856

*Terms of use:*

This article is made available under terms and conditions as specified in the corresponding bibliographic description in the repository

*Publisher copyright*

(Article begins on next page)

18 November 2026

Journal of Power Sources 663 (2026) 238856

Contents lists available at ScienceDirect

Journal of Power Sources

journal homepage: www.elsevier.com/locate/jpowsour

# Sustainable solid-state polymer electrolyte based on PEO-Xanthan gum blend for enhanced lithium-metal batteries

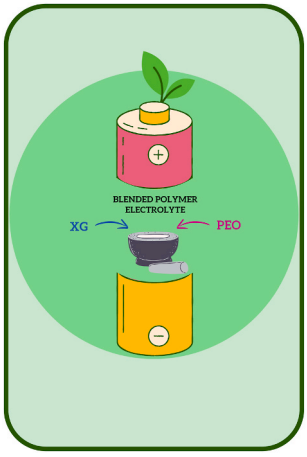
Asia Patriarchi [a], Hamideh Darjazi [b,c], Maddalena Barcaioni [a], Luca Minnetti [a], Alberto Fina [b], Andrei Filippov [d], Faiz Ullah Shah [d], Oleg N. Antzutkin [d], Miguel Ángel Muñoz-Márquez [a,c,*], Francesco Nobili [a,c,**]

[a] School of Science and Technology, Chemistry Division, University of Camerino, via Madonna delle Carceri - ChIP, Camerino, MC, 62032, Italy
[b] GAME Lab, Department of Applied Science and Technology (DISAT), Politecnico di Torino, C.so Duca degli Abruzzi 24, Torino, TO, 10129, Italy
[c] National Reference Centre for Electrochemical Energy Storage (GISEL), Via Giusti 9, Firenze, FI, 50121, Italy
[d] Chemistry of Interfaces, Department of Civil and Environmental Engineering, Luleå University of Technology, Luleå, SE-97187, Sweden

## HIGHLIGHTS

- PEO/Xanthan Gum-based Solid Polymer Electrolytes are synthesized and characterized.
- The most suitable composition is given by a blend PEO:XG 80:20, with LiTFSI salt.
- Transport properties are assessed by NMR and electrochemical methods.
- The electrochemical stability window lies in the 0.01 V < E < 4.8 V.
- The SPE is compatible with metal Li anode and olivine-type cathodes (LFP and LFMP).

## GRAPHICAL ABSTRACT




## ABSTRACT

Despite their widespread adoption, LIBs are still facing several challenges, mainly related with safety concerns of conventional electrolytes that are currently limiting their practical use. Solid-state polymer electrolytes (SPEs) represent a promising alternative to produce safer devices, as they offer higher flexibility and energy density, easy processability, non-flammability and improved mechanical strength, even if they often suffer from low ionic conductivity at room temperature. To address the latter issue, the development of novel SPEs based on a blend of polyethylene oxide (PEO) and Xanthan gum (XG), a natural polysaccharide with notable mechanical and rheological properties, is proposed. In this study, the thermal, physical, and electrochemical properties of the PEO-XG blends were investigated,

This article is part of a special issue entitled: In memory of Professor Bruno Scrosati published in Journal of Power Sources.

* Corresponding author. School of Science and Technology, Chemistry Division, University of Camerino, via Madonna delle Carceri - ChIP, Camerino, MC, 62032, Italy.

** Corresponding author. School of Science and Technology, Chemistry Division, University of Camerino, via Madonna delle Carceri - ChIP, Camerino, MC, 62032, Italy.

*E-mail addresses:* miguel.munoz@unicam.it (M.Á. Muñoz-Márquez), francesco.nobili@unicam.it (F. Nobili).

https://doi.org/10.1016/j.jpowsour.2025.238856
Received 30 June 2025; Received in revised form 16 October 2025; Accepted 13 November 2025
Available online 18 November 2025
0378-7753/© 2025 The Authors. Published by Elsevier B.V. This is an open access article under the CC BY license (http://creativecommons.org/licenses/by/4.0/).

aiming to assess their potential as electrolyte for all solid-state lithium metal batteries. Improved ionic conductivity, electrochemical stability window and cycling stability are achieved, confirming the effectiveness of XG incorporation. The most promising electrolyte formulation was studied using self-diffusion $^{7}$Li pulse-field-gradient (PFG) NMR measurements and different temperatures and further evaluated in full-cell configurations employing two olivine-type cathodes (LFP and LMFP). When paired with a lithium manganese iron phosphate (LMFP) cathode and cycled over an extended voltage window of 2.5–4.5 V, the cell demonstrates high specific capacity and excellent capacity retention, maintaining stable performance for at least 750 cycles.

## 1. Introduction

The pressing need for sustainable energy storage solutions is highlighted by the exponential rise in global energy demand, coupled with escalating concerns about pollution and fossil fuels emission that are leading to a rapid environmental degradation [1,2]. Thus, one of the greatest challenges of this century is to meet the world's ever-increasing energy requirements without compromising the sustainability and the affordability of the employed processes [3–5]. Since their commercial debut in 1991, lithium-ion batteries (LIBs) have emerged as a highly promising solution, which became dominant across multiple fields such as portable electronics and electric vehicles [6].

The huge success of LIBs is nested in their remarkable properties including high energy density, prolonged cycle life, low self-discharge and elevated power density [7–10]. However, the use of conventional liquid electrolytes, which typically consist of highly flammable and volatile organic solvents [11,12], result in limited practical application of LIBs due to significant safety concerns. Moreover, liquid electrolytes significantly impact the overall cell performance, narrowing the operating temperature range and voltage stability window, while also increasing the leakage risk [13,14]. These drawbacks have prompted the exploration of alternative solutions to enhance the overall safety and energy density of the battery. Solid electrolytes have emerged as promising alternatives and, in particular, polymer-based solid electrolytes (SPEs) seem particularly appealing due to their excellent mechanical strength and easy processability [15–17]. The choice of a suitable polymeric matrix is a crucial consideration for the development of SPEs: while various polymers, including polyvinylidene fluoride (PVDF) [18–20], polyvinyl alcohol (PVA) [21,22], and poly(methyl methacrylate) (PMMA) [18,23], have been extensively studied, polyethylene oxide (PEO) [24–27] has emerged as the best candidate thanks to its outstanding properties, such as remarkable thermal stability, high flexibility, water solubility, low toxicity and cost-effectiveness [28,29].

However, the main challenge of solid polymer electrolytes remains the low ionic conductivity at room temperature [30,31]. To address this limitation, several methods have been explored, including the incorporation of active or passive fillers within the electrolyte to enhance lithium ion diffusion and improve mechanical properties [32–36], as well as the utilization of plasticizers to facilitate polymer chain movement and thus reduce crystallinity [37,38]. Recently, the idea of combining two distinct polymer matrices has emerged as a promising field of study [39,40]. This strategy enables tuning the characteristics of the individual polymers, thereby facilitating the development of materials with optimized conductivity, electrochemical stability, and mechanical properties [41,42]. In this context, biopolymers represent an excellent sustainable choice, as they are derived from renewable sources such as plants, animals, or microorganisms. Being non-toxic and water-soluble, they offer environmentally friendly alternatives with tunable physicochemical properties that can significantly enhance both performance and eco-compatibility of next-generation energy storage systems [43–45]. In particular, Xanthan gum (XG) is a complex exopolysaccharide characterized by the presence of trisaccharide side chains made of a d-glucuronic acid ring sandwiched between d-mannose acetate ramifications, with a d-mannose pyruvate terminal ring [46,47]. XG is produced through the aerobic fermentation of *Xanthomonas campestris* and it tends to form dense gels with water, which has allowed its use for several industrial applications, including those related to the cosmetics, food and pharmaceuticals [48].

In this study, novel solid-state polymer electrolytes, made of PEO/LiTFSI (EO/Li 1:21) membranes in which different percentages of Xanthan gum were incorporated to form a blend, are compared with a SPE made of bare polyethylene oxide (PEO) and lithium bis(trifluoromethanesulfonyl)imide (LiTFSI) (EO/Li 21:1). The physical characteristics of the SPEs were deeply investigated by means of thermal gravimetric analysis (TGA), scanning electron microscopy (SEM), differential scanning calorimetry (DSC), $^{7}$Li Pulsed-Field-Gradient Nuclear Magnetic Resonance (PFG-NMR), Raman and Fourier transform infrared spectroscopy (FTIR). Additionally, electrochemical techniques such as impedance spectroscopy (EIS), cyclic voltammetry (CV), linear sweep voltammetry (LSV), chronoamperometry (CA), and galvanostatic cycling with potential limitation (GCPL) were employed. Furthermore, once the optimal blend proportion had been identified, the electrolyte was first evaluated in full-cell configuration using lithium metal as anode and lithium iron phosphate (LFP) as cathode, to assess its compatibility with the cathodic material. Then, LFP was substituted by LMFP to extend the upper voltage limit to 4.5 V and more rigorously evaluate the performance of the electrolyte under harsher electrochemical conditions, including increased voltage stress and higher current densities.

## 2. Experimental section

Lithium bis(trifluoromethansulfonyl)imide (LiTFSI), poly(ethylene oxide) (PEO, average Mw ~ 4,000,000 nominal), Xanthan gum (XG), conductive carbon (Super C65), *N*-methyl pyrrolidone (NMP) and lithium iron phosphate ($LiFePO_4$, LFP) were procured from Sigma-Aldrich. PVDF was obtained from Solvay. Lithium iron manganese phosphate ($LiMn_{0.6}Fe_{0.4}PO_4$, LMFP) was purchased from Gelon. All chemicals were utilized without any additional purification; however, both the polymers and LiTFSI salt underwent vacuum drying at 50 °C overnight to eliminate any traces of absorbed water.

**Preparation of PEO/XG/LiTFSI electrolytes:** Blended PEO/XG/LiTFSI solid polymer electrolytes were synthesized using a completely solvent-free method. Dried PEO was manually mixed with varying percentages of XG (5 %, 10 %, 20 %, and 30 % in weight) in a mortar, followed by the addition of LiTFSI salt (EO/Li = 21:1) under an inert argon atmosphere. To ensure thorough homogenization, the mixture was transferred to an agate jar and ball-milled at 450 rpm for 30 min (ball-to-powder ratio of 30:1). The resulting powder blend was then placed between two Teflon sheets and hot-pressed at 70 °C for 2 min, forming a uniform, self-standing white film. The membranes were carefully peeled off, cut into 16 mm disks, and transferred to a Büchi oven at 50 °C for 15 h to eliminate residual moisture. Finally, the prepared electrolytes were stored in an argon-filled glove box. Four novel SPE formulations incorporating XG were synthesized, along with a pristine PEO/LiTFSI membrane (without XG) to serve as a reference for evaluating the impact of XG on the electrolyte properties.

**Preparation of LFP and LMFP cathode:** Commercial lithium iron phosphate and lithium iron manganese phosphate powders were selected as the active materials and combined with conductive carbon C65 and PVDF in a ratio of 8:1:1, utilizing *N*-methyl pyrrolidone (NMP) as solvent. The resulting black slurries were stirred for 6 h to achieve homogeneous viscous suspensions, which were then cast by means of a doctor blade onto aluminum foil that served as current collector. Afterward, the laminates were dried overnight at 60 °C and cut into 9 mm disk electrodes (0.636 $cm^2$ electrode surface, with a mass loading of

approximately 5–6 mg $cm^{-2}$), pressed at 5 tons for 30 s, and further dried in a Büchi oven at 120 °C for 4 h. Finally, the electrodes were weighed and transferred into an argon-filled glovebox.

**Characterization and measurements:** The morphology of the electrolytes' surfaces was studied using a scanning electron microscope (Zeiss Sigma 300 FM - SEM). The LiTFSI salt distribution within the polymeric matrices was investigated by means of Electron Probe Micro Analysis (EPMA) performed with energy-dispersive X-ray detector (EDX). The nature of the polymers' functional groups was confirmed through Fourier-transform infrared spectroscopy (FTIR) analysis using a PerkinElmer Frontier instrument, aiming to assess the potential formation of new bonds or interactions among the components of the membrane. X-ray diffraction (XRD) was employed to analyze the structure of the electrolyte membrane and of the single components using a Bruker D6 Phaser (40 kV, 15 mA) with non-monochromatic Cu Kα radiation (λ = 1.5408 Å) and adopting a Si-strip SSD160-2 detector with 160 channels. Scans were performed in Bragg-Brentano mode in the 2θ range from 5° to 75° at a rate of 0.4 s $step^{-1}$ and a step size of 0.02°. In addition, XRD patterns of LFP and LMFP powders were achieved as above described in the 15°–60° 2θ range. To ensure the thermal stability of the SPEs, thermal gravimetric analysis (TGA) was conducted in the temperature range from 30 °C to 550 °C under a nitrogen atmosphere, with a heating rate of 10 °C $min^{-1}$, utilizing a PerkinElmer STA6000 TGA-DTA instrument. Differential Scanning Calorimetry (DSC Q20 TA Instruments) was used for the determination of the glass transition temperature, melting point, melting enthalpy and crystallization temperature of the samples. The SPEs were analyzed in the −65 °C – 100 °C temperature range under nitrogen flow and with a heating and cooling rate of 10 °C $min^{-1}$.

Electrochemical impedance spectroscopy (EIS) in potentiostatic mode and galvanostatic cycling with potential limitation (GCPL) were performed at 65 °C in symmetric cell configuration to assess, respectively, the electrolyte resistance and cycling behavior of the membranes over a minimum of 50 stripping/plating cycles with a current density of 0.05 mA $cm^{-2}$. The stability of the most promising electrolyte was further examined over an extended number of cycles. Moreover, the change in electrolyte resistance and any increase in overall cell resistance were monitored by recording impedance measurements daily over the course of one month.

The ionic conductivity (σ) was determined via impedance spectroscopy within the frequency range of 101 kHz to 5 mHz recording an impedance spectrum at intervals of 5 °C across a temperature range 25 °C–70 °C. Custom Teflon O-rings with dimensions of 16 mm outer diameter and 9 mm inner diameter was utilized to ensure uniform thickness of the electrolytes. Stainless steel (SS) spacers served as blocking electrode.

For the calculation of σ, the following formula was applied:

$$\sigma = \frac{L}{RA}$$

where $L$ corresponds to the membrane's thickness, $R$ is the bulk resistance obtained from the fitting of impedance measurement and $A$ is contact area.

$Li^+$ transference number at four different temperatures (45 °C, 55 °C, 65 °C and 75 °C) was determined by Bruce-Vincent-Evans method in lithium symmetric cell configuration (Li|SPE|Li) [49]:

$$\tau^+ = \frac{i_{ss}}{i_0} \times \frac{(\Delta V - R_0 i_0)}{(\Delta V - R_{ss} i_{ss})}$$

$i_0$ = initial state current
$i_{ss}$ = steady-state current
$R_0$ = the initial resistance
$R_{ss}$ = steady-state resistance
$\Delta V$ = applied potential

The electrochemical stability window was studied through linear sweep voltammetry (LSV), cyclic voltammetry (CV) and chronoamperometry (CA), all the measurements were performed at 65 °C with a scan rate of 0.1 mV $s^{-1}$. For these tests, a working electrode (WE) was fabricated by blending conductive carbon (C65) with PVDF in an 8:2 wt ratio. This mixture was then cast onto both aluminum and copper current collectors and used to determine the anodic and cathodic stability, respectively.

The $^7Li$ NMR experiment was performed using Bruker Ascend Aeon WB 400 (Bruker BioSpin AG) NMR spectrometer. The working frequency for $^7Li$ was 155.56 MHz. Lithium spectra were externally referenced relative to the $^7Li$ resonance of $LiNO_3$ (aq) (−0.147 ppm). NMR data was processed using Bruker Topspin 3.5 software. For diffusion measurements a Diff50 Pulsed-Field-Gradient (PFG) probe was used. The diffusion decays (DD) were recorded using the stimulated echo (StE) pulse sequence. For a single-component diffusion, the form of the DD can be described as shown in Equation (1) [50]:

$$A(\tau, \tau_1, g, \delta) \propto \exp\left(-\frac{2\tau}{T_2} - \frac{\tau_1}{T_1}\right) \exp\left(-\gamma^2 \delta^2 g^2 D t_d\right) \quad (1)$$

Here, $A$ is the integral intensity of the NMR signal, $\tau$ and $\tau_1$ are the time intervals in the pulse sequence; $\gamma$ is the gyromagnetic ratio for magnetic nuclei; $g$ and $\delta$ are the amplitude and the duration of the gradient pulse; $t_d = (\Delta - \delta/3)$ is the diffusion time; $\Delta = (\tau + \tau_1)$. $D$ is the self-diffusion coefficient. In the measurements, $\delta$ was in the range of (0.5–3) ms, $\tau$ was in the range of 1–4 ms, and $g$ varied from 0.06 up to 29.73 T $m^{-1}$. Diffusion time $t_d$ was 20 ms. The recycle delay during accumulation of signal transients was 3.5 s. Each experiment was repeated at least three times. Non-linear least squares regression was used to fit the experimental data with Equation (1) to extract $D$ values.

All the electrochemical tests were conducted using 9 mm electrodes and 16 mm electrolyte membranes in CR2032 coin-type cells, which were assembled in an argon-filled glovebox (Jacomex GP Campus with $O_2$ and $H_2O$ levels <0.8 ppm) to ensure an inert atmosphere.

## 3. Results

### 3.1. Thermal analysis

In order to assess the thermal stability of the electrolytes, thermogravimetric analysis was performed heating the samples from 30 °C to 550 °C under a nitrogen atmosphere. The results are shown in Fig. 1a. The pristine membrane, which was synthesized without XG addition (EO/Li 21:1), was taken as a reference in order to better understand the degradation pathway of the blend polymer electrolytes. As previously reported, the pristine sample exhibited a single-step decomposition with an onset temperature of approximately 433 °C and complete decomposition occurring at 480 °C, together with a first weight loss (corresponding to 2.7 %) attributable to the elimination of adsorbed water, which was fully removed up to approximately 150 °C [51–53].

When XG was added, three distinct weight loss events were observed. The first corresponds to the loss of adsorbed water, occurring between 60 °C and 150 °C, like the pristine membrane [54]. As reported in Table 1, as the percentage of the copolymer increases, the DTA peak is shifted to lower values, indicating that the loss of moisture starts at lower temperature. At the same time, the weight loss is more pronounced, suggesting the hygroscopic nature of Xanthan moieties. The second thermal degradation process, absent in the pristine membrane, corresponds to the decomposition of Xanthan's polysaccharide backbone, occurring in the temperature range from 250 °C to 360 °C [55]. Furthermore, the gradual increase in the percentage of XG within the blend results in a corresponding increase in weight loss, which can be attributed to the polymer degradation. This trend is accompanied by a reduction in the onset temperature, indicating that the thermal stability of the blended polymer electrolyte diminishes with higher XG content,

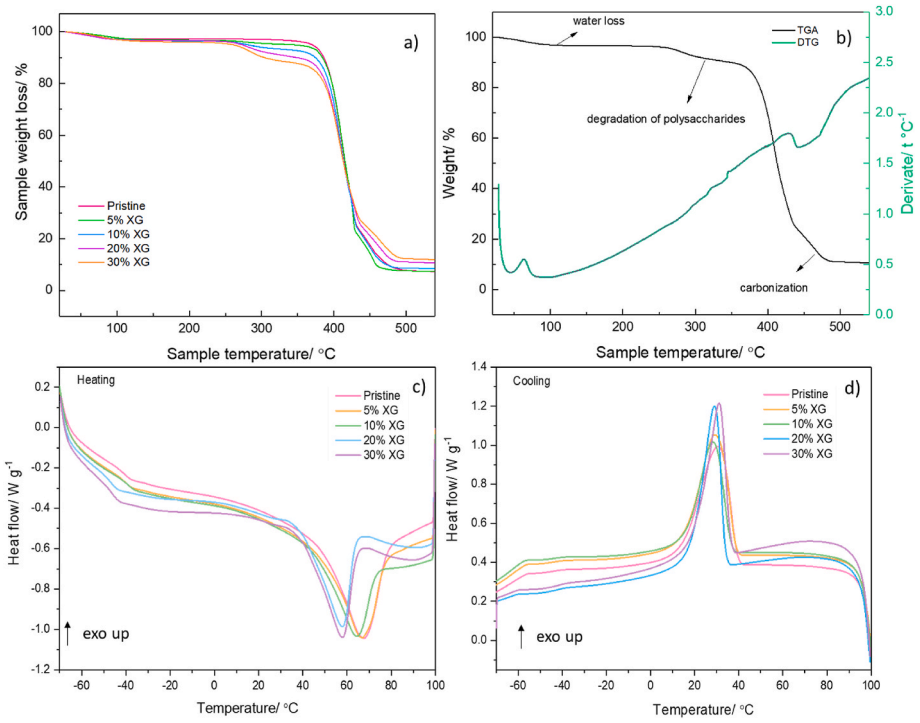



**Fig. 1.** (a) TGA curves of all the electrolytes recorded in the temperature range of 25–550 °C under a nitrogen atmosphere. (b) Details of TGA and DTA curves for the 20 % XG electrolyte. (c) Heating and (d) cooling differential scanning calorimetry profiles recorded from −65 °C to 100 °C temperature range under nitrogen flow.

**Table 1**
Weight loss associated with decomposition steps of the samples according to TGA curves.

| Sample | 1st loss | | 2nd loss | | 3rd loss | |
|---|---|---|---|---|---|---|
| | *Onset Temperature (°C)* | *Weight loss (%)* | *Onset Temperature (°C)* | *Weight loss (%)* | *Onset Temperature (°C)* | *Weight loss (%)* |
| **Pristine** | 65 | 2.7 | none | none | 430 | 90.5 |
| **PEO-XG 5 %** | 65 | 2.9 | 270 | 5.5 | 428 | 91 |
| **PEO-XG 10 %** | 64 | 3.4 | 265 | 8 | 430 | 90 |
| **PEO-XG 20 %** | 63 | 3.4 | 255 | 11 | 433 | 88 |
| **PEO-XG 30 %** | 61.5 | 3.5 | 250 | 13 | 435 | 87 |

as illustrated in Table 1. Lastly, the final weight loss is likely attributed to a combination of several degradation pathways, as evidenced by multiple peaks present in the DTA. This includes the carbonization of Xanthan residues and the random breakage of PEO chains, leading to the formation of side products such as alkenes and ethers [39,56,57].

Fig. 1b provides a detailed overview of degradation processes of a representative PEO-XG electrolyte, which was further analyzed by DTA, allowing a deeper understanding of the thermal stability and degradation behavior of the SPE.

Fig. 1c and d shows the thermograms obtained from DSC analysis performed on various compositions of the blended polymer electrolyte in comparison with the pristine electrolyte. The results are summarized in Table 2. A single melting peak between 55 °C and 65 °C is observed for all the electrolytes, in good agreement with the results obtained for the sample where only PEO is present. The pristine membrane exhibits the highest melting temperature at approximately 64.5 °C, aligning well with reported literature values [36,58]. Notably, the incorporation of XG has led to a reduction in the melting temperature of the electrolyte. This effect is likely associated with enhanced chain mobility, which consequently lowers the energy required for melting. Specifically, when 20 % XG is added, the electrolyte exhibits a melting temperature of approximately 57.7 °C, nearly 7 °C lower than that of the pristine electrolyte.

**Table 2**
Electrolytes values of melting temperature ($T_m$), glass transition temperature ($T_g$), crystallization temperature ($T_c$) and enthalpy of melting (ΔH melting) obtained from DSC analysis.

| Sample | $T_m$ (°C) | $T_g$ (°C) | $T_c$ (°C) | ΔH melting (J/g) |
|---|---|---|---|---|
| **Pristine** | 64.5 | −41.4 | 30.4 | 62.4 |
| **PEO-XG 5 %** | 62.7 | −41.3 | 29 | 58.9 |
| **PEO-XG 10 %** | 62 | −41.8 | 28.1 | 52.9 |
| **PEO-XG 20 %** | 57.6 | −45.7 | 29 | 46.5 |
| **PEO-XG 30 %** | 58.1 | −45 | 31 | 53.1 |

A similar trend could be underlined for the glass transition temperatures ($T_g$) of the samples: the $T_g$ values progressively decrease as the copolymer content increases. This downward shift in $T_g$ may reflect an enhanced segmental mobility of the polymer chains, suggesting that the addition of XG contributes to a more amorphous and flexible matrix structure. In particular, the PEO-XG 20 % composition displays the most pronounced reduction in $T_g$, with a decrease of approximately 3 °C compared to the pristine membrane. Moreover, XG appears to have a weak influence on the crystallization process; although the crystallization temperature shifts only slightly, the resulting crystals are likely smaller and therefore less thermally stable. This interpretation is supported by the observed decrease in the enthalpy of fusion (ΔH melting), especially for the best-performing sample.

This data further suggests that the increased presence of the

copolymer acts as an internal plasticizer, improving the overall flexibility of the polymeric matrix.

### 3.2. Structural and morphological characterization

FTIR spectroscopy was employed to investigate the electrolytes' vibration modes, which are active in the infrared spectral region, as depicted in Fig. 2a. For comparison, the vibrational modes of the two pristine polymers have been reported in Table S1.

FTIR spectroscopy represents a valuable tool, enabling the investigation of new bond formation and interactions among the blend components and thus providing insights into structural changes. In particular, a comparison of the spectral patterns reveals a slight peak shift as the percentage of copolymer increases. This suggests a possible modification of the chemical environment surrounding the functional groups, which may influence their stretching frequencies, as better illustrated in Fig. 2a. It has been previously proposed that carboxylate groups of Xanthan gum can interact with hydroxyl groups of molecules such as ethylene glycol through an esterification reaction [46,59]. Further confirmation of the high chemical affinity and compatibility of the two polymers can be obtained by examining the OH stretching region, in which a broad band at around 3475 $cm^{-1}$ and a less intense one at 3282 $cm^{-1}$ could be observed, as illustrated in Fig. 2b. The most intense band arises from the OH groups of PEO, instead the other (3282 $cm^{-1}$) is attributed to XG structure. Interestingly, the OH band associated with PEO shows a marked decrease in intensity as the copolymer percentage increases. This behavior suggests a progressive reduction in free OH groups from PEO, likely resulting from increased interactions or hydrogen bond formation with the copolymer. Notably, upon the addition of 20 % XG, the 3475 $cm^{-1}$ peak reaches its lowest intensity, indicating the strongest intermolecular interactions between the two polymers at this composition.

Further insight can be gained from the analysis of the spectral region between 1350 $cm^{-1}$ and 1750 $cm^{-1}$ as illustrated in Fig. 2c. In this region, distinct changes in the characteristic vibrational modes provide evidence of interactions between the two polymers. Notably, the peaks associated with the carboxyl groups of XG, observed at approximately 1600 $cm^{-1}$ and 1710 $cm^{-1}$ in its pristine spectrum, almost entirely disappear in the blend. Additionally, a reduction in the peak around 1400 $cm^{-1}$ (CO stretching deformations in XG) further supports the occurrence of intermolecular interactions between the carboxyl groups of XG and the hydroxyl groups of PEO, which may enhance the compatibility between the two polymers [60].

The morphology of the synthesized SPEs was evaluated by means of SEM analysis, as shown in Figure S1 a-d (see Supporting Information). Although none of the electrolytes displayed signs of cracking, XG 20 % sample demonstrated notably greater structural uniformity characterized by a smooth, defect-free surface, which may promote improved contact between the electrolyte and electrode, potentially enhancing overall cell performance. Furthermore, for the XG 20 % sample the SEM analysis has been integrated by the corresponding elemental mapping obtained by EPMA (Fig. 3), to verify the uniform distribution of both the polymer matrix and lithium salt within the solid polymer electrolyte. Specifically, carbon and oxygen (Fig. 3b and c), indicative of the polymer backbones, are consistently dispersed across the all surface. Sulfur and fluorine (Fig. 3d and e), attributable to LiTFSI salt, are evenly distributed with no evidence of aggregation, confirming the membrane homogeneity. The X-ray diffraction patterns of the 20 % XG membrane, along with those of its individual components, are presented in Fig. 3f. The membrane (blue pattern) exhibits distinct features, particularly in the 15°–25° 2θ range, along with a broad baseline signal. This broad contribution is likely associated with the amorphous nature of the Xanthan gum copolymer, as evidenced by the pure XG pattern shown for comparison. However, the diffractogram of the 20 % XG membrane appears only partially ascribable to the single species forming the membrane, while only few peaks of PEO (orange diffractogram) and LiTFSI salt (green diffractogram) may be identified, thus indicating the formation of a complex crystalline structure due to the rearrangement of

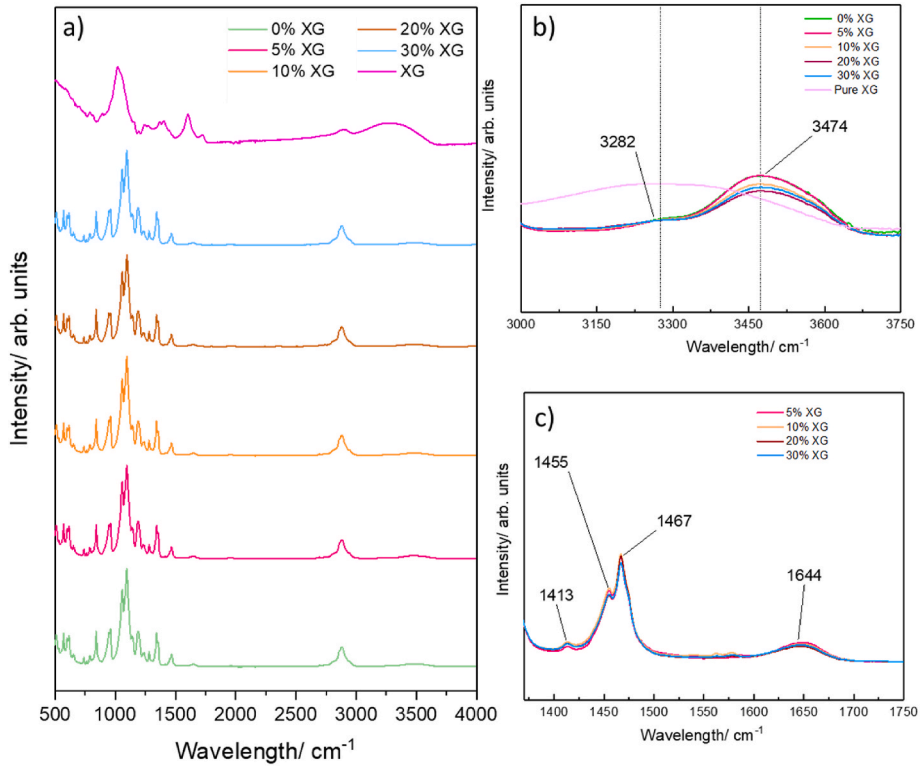



**Fig. 2.** (a) FTIR spectra of the synthesized electrolyte in the 4000-400 $cm^{-1}$ range compared to the pristine electrolyte and pure XG. (b) Details of the OH vibrational mode for all the electrolytes and pristine XG. (c) Zoomed-in view of the spectral region between 1250 and 1750 $cm^{-1}$.

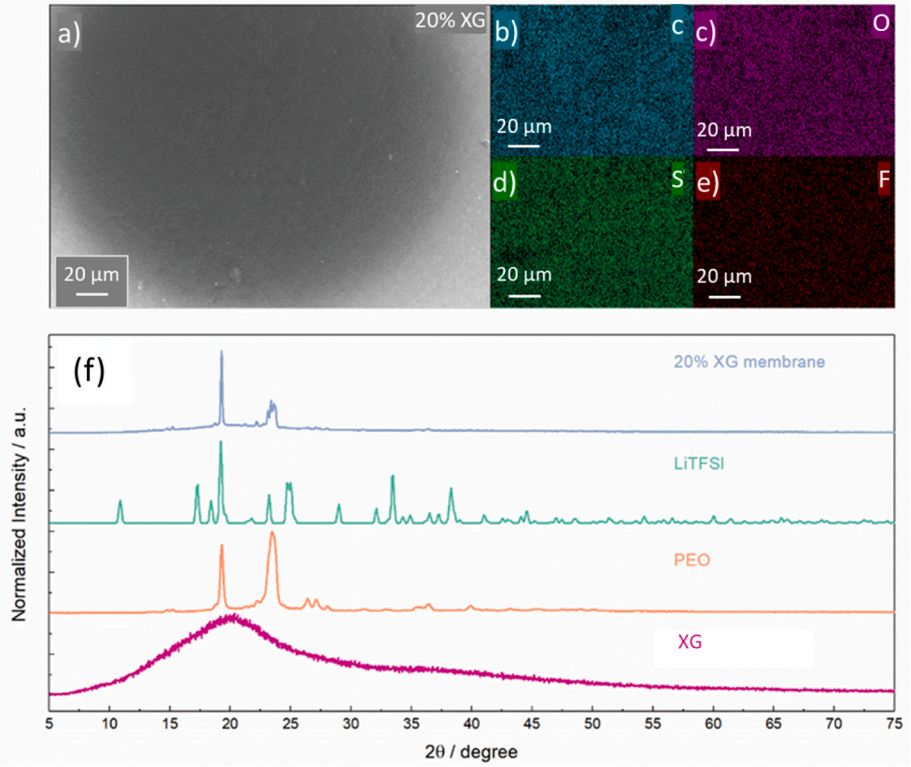



**Fig. 3.** (a) SEM micrograph and elemental mapping of (b) carbon, (c) oxygen, (d) sulfur, and (e) fluorine performed on 20 % XG electrolyte. (f) XRD pattern recorded for 20 % XG electrolyte and for the single components.

the components during the synthesis [61,62]. Indeed, as already reported for PEO-based polymer electrolytes, both the homogeneous dispersion of the components and the formation of a structure which may differ from the one of the single components, could lead to an improvement of the mechanical and electrochemical properties of the final electrolyte [63,64].

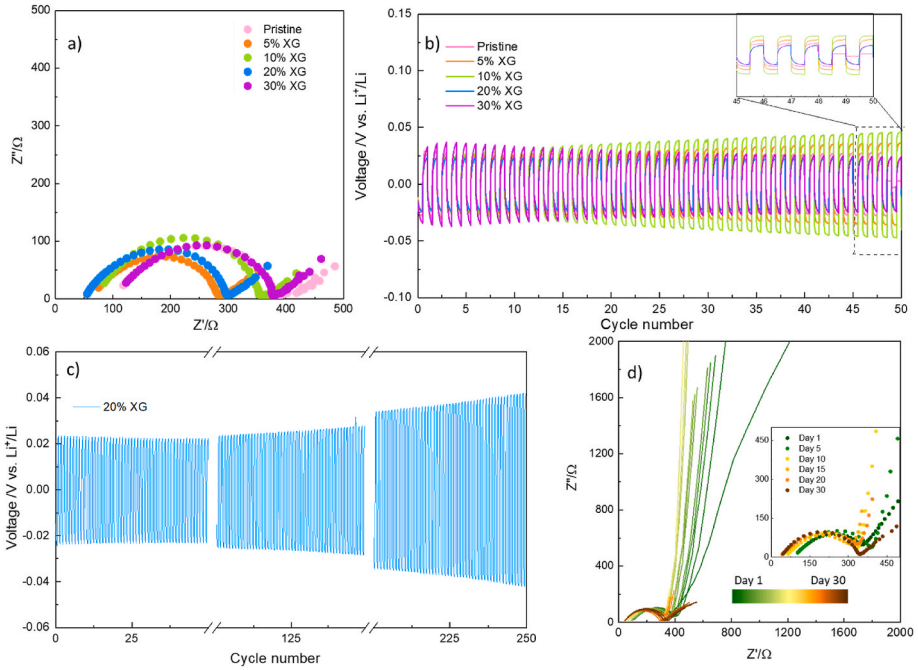



**Fig. 4.** (a) EIS measurements for PEO LiTFSI (EO/Li 21:1) membranes with different XG ratios at OCV; (b) 50 galvanostatic plating/stripping cycles of symmetrical Li|SPE|Li cells at 65 °C with a current density of 0.05 mA $cm^{-2}$. The inset displays an enlarged view of the last five cycles; (c) Galvanostatic plating/stripping long cycling performances of a symmetrical Li|20 % XG|Li cell and (d) Resistance evolution monitored by impedance spectroscopy, with one measurement recorded per day over the course of one month.

### 3.3. Electrochemical performances

**EIS and stripping/plating test:** Electrolyte resistivity, together with cycling stability, is a critical parameter that must be optimized to ensure adequate cell performance. To assess the electrochemical properties of the synthesized SPEs, symmetric Li|SPE|Li coin cells were assembled and tested at 65 °C. Electrochemical impedance spectroscopy was performed over a frequency range 101 kHz to 5 mHz, and the resulting Nyquist plots are presented in Fig. 4a. The spectra have been modelled using the equivalent circuit method through a non-linear least squares (NLLS) fitting protocol with the RelaxIS 3 software (rhd instruments, Darmstadt, Germany) [65]. According to Boukamp's notation, the equivalent circuit chosen was $R_e(R_iC_i)Q_w$ to describe all the contributions to the dispersions: $Li^+$ ion migration through the solid electrolyte; contact resistance and Li metal interface resistance, together with the double-layer capacitances; Warburg-type bulk solid-state diffusion [66]. During the fitting of the EIS patterns, the capacitive elements ($C_i$) were replaced with constant-phase elements ($Q_i$) in order to consider also surface irregularities or roughness. The results of the fitting are presented in Table S2.

According to the data reported in Table S2, all the electrolytes presented have a comparable $R_{overall}$ value, which is consistently lower than that of the pristine membrane, likely due to a less resistive behavior in the modified formulations. The incorporation of 20 % XG proved to be particularly effective, resulting in the lowest electrolyte resistance, as evidenced by a lower intercept with the real axis in Nyquist dispersion. However, the overall electrolyte resistance exhibits a non-monotonic trend, reaching a minimum at 20 % XG. This behavior likely reflects a balance between bulk ion transport and microstructural effects, as reported in previous studies [46,48]. Moderate XG content enhances the amorphous fraction and polymer segmental motion, promoting $Li^+$ conduction and good electrode contact, whereas high XG loadings may introduce microphase separation or tighter polymer packing, hindering homogeneous ion transport pathway.

The electrolyte resistivity has been further evaluated by assessing the SPEs overpotential by means of stripping and plating tests applying a current density of 0.05 mA $cm^{-2}$, as shown in Fig. 4b. The pristine membrane experienced dendrite formation after 48 cycles, resulting in a drop in polarization followed by short circuit of the cell, as better illustrated in the inset. In contrast, the blended membranes showed no signs of failure over 50 cycles. However, the formulation containing 30 % XG required several activation cycles to achieve stable performance, while the 10 % XG blend displayed relatively poor cycling stability, as evidenced by a progressive increase in overpotential during cycling. Consistently with impedance spectroscopy results, the 5 % and 20 % XG membranes exhibited similar trends during the initial cycles. The 20 % XG membrane not only demonstrated the lowest overpotential. but also maintained superior cycling stability over time. In comparison, the 5 % XG sample experienced more pronounced polarization and a gradual rise in resistance, indicating reduced long-term interfacial stability.

To deeper investigate the stability of the most promising electrolyte, the long cycling performance of the blend containing 20 % XG is shown in Fig. 4c. No dendrites formation or dead lithium was detected, successfully avoiding short circuit or failure for more than 250 cycles. The cell overpotential resulted to be quite stable, with only a slight increase after 200 cycles, thus confirming the satisfactory properties of the SPE with 20 % XG. Furthermore, the temporal evolution of the electrolyte and interfacial resistances was evaluated by monitoring the impedance response over a one-month period. One EIS spectrum was recorded each day, and the corresponding Nyquist plots are shown in Fig. 4d, with selected spectra highlighted for comparison (inset). The results suggest a remarkable stability of the membrane, with a slight decrease in electrolyte resistance over time, which could be attributed to a gradual activation or reorganization of the polymer structure, thereby enhancing ion transport and overall membrane performance. Additionally, the evolution of the interfacial resistance results in a stable semicircle diameter after the initial period, thus validating the suitability of the 20 % XG blend as a solid polymer electrolyte for lithium-ion batteries.

Arrhenius plots of electrolyte conductivity were obtained by reporting the trends of $1/R_e$ at different temperatures for pristine and XG-modified membranes (Fig. 5a). The plot could be divided into two distinct regions which are separated by a change in slope: the first ranging from room temperature to approximately 60 °C, while the second region begins beyond the melting point of the electrolyte (see Table 2). The data set recorded in the temperature range of 25 °C–55 °C was fitted using a linear model, as it adhered closely to the classical Arrhenius behavior [67]. Near to the knee of the Arrhenius plot, a phase transition from solid to fluid occurred, increasing the degree of freedom of the polymeric matrix and consequently reducing the energy barrier for ion transport. Above 60 °C, the SPEs exhibited a more pronounced Vogel-Tammann-Fulcher (VTF) behavior, indicative of the increased molecular mobility and non-Arrhenius dynamics associated with the melted electrolyte phase [68]. The activation energy of the system was evaluated both before and after the melting point, as summarized in Table 3.

The higher activation energy ($E_a$) exhibited at temperatures lower than melting points of SPEs does suggest that the polymers are characterized by an increased matrix stiffness, which potentially restricts chain mobility and limits lithium-ion transport. However, the incorporation of XG in PEO results in a plasticizing effect within the polymer electrolyte, leading to a reduction in $E_a$ compared to the pristine electrolyte in accord with the DSC results (see Fig. 1c and Table 2). Interestingly, the $E_a$ trend at temperatures higher than the melting points of SPEs correlates well with the XG content, as an increase in the copolymer concentration does lead to a higher ionic conductivity and to a corresponding decrease in the activation energy. At all temperatures in this study, the pristine membrane exhibited both the lowest ionic conductivity and the highest activation energy of the electrolyte conductivity before and after the melting temperature of the SPE.

The transference number of the electrolytes was calculated using the Bruce-Vincent-Evans method: two impedance spectra were recorded before and after applying a $\Delta V = 30$ mV for 1 h on a Li|SPE|Li symmetric cell. In good agreement with the literature, the transport number rises as the operating temperature increases, as shown in Table 3. This behavior can be attributed primarily to anion immobilization resulting from the thermally induced amorphization of the polymer matrix. Thermal activation enhances polymer chain mobility, promoting more effective anion solvation and thereby reducing ion pairing. In addition, the increased amorphous character of the matrix provides greater free volume, which facilitates polymer segmental motion and favors lithium salt dissociation. As a result, $Li^+$ cations can migrate more efficiently through the amorphous domains via a combination of long-range transport and localized hopping mechanisms [69,70].

### 3.4. Electrochemical stability window

Achieving a wide electrochemical stability window while preventing premature electrolyte decomposition is essential for evaluating compatibility with cathode materials and ensuring feasibility in full-cell configurations. To investigate the stability of the solid polymer electrolytes, linear sweep voltammetry, cyclic voltammetry and chronoamperometry tests were performed using working electrodes composed of conductive carbon and PVDF (8:1 wt ratio) cast onto aluminum and copper current collectors, for anodic and cathodic assessments, respectively.

The anodic stability window was first evaluated using linear sweep voltammetry in the 3–5.5 voltage range. As displayed in Fig. 5b, all curves exhibited a stable, flat profile up to 4.5 V, beyond which a degradation peak appeared, likely attributed to the oxidation of the polymeric matrix. Notably, the incorporation of the copolymer enhances the stability window, extending it beyond that of the pristine membrane. This improvement may be attributed to the decrease of free, reactive

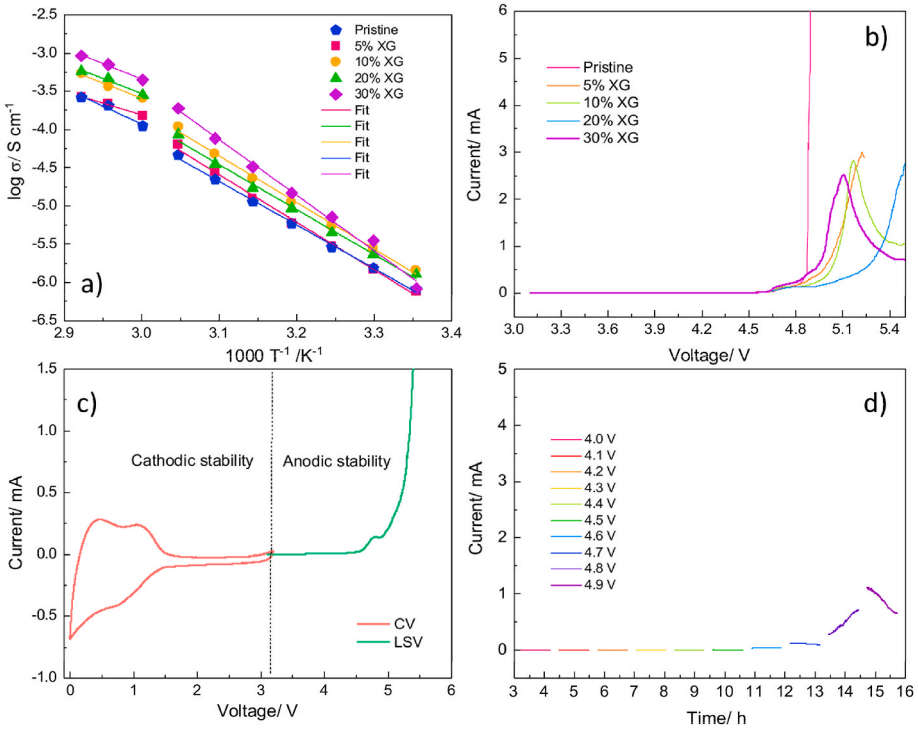



**Fig. 5.** Electrochemical characterization of the electrolytes: (a) Arrhenius plots for ionic conductivity of the synthesized electrolytes in comparison with pristine membrane, with corresponding linear fits before and after melting point of the polymer, (b) Linear sweep voltammetry in anodic region performed at 65 °C in a Li|SPE|WE cell configuration, (c) Linear sweep voltammetry and cyclic voltammetry in anodic and cathodic regions, respectively, recorded on a Li|20 %XG|WE cell configuration. (d) Chronoamperometry curves recorded on a Li|20 %XG|WE cell configuration used for a more accurate determination of the anodic limit.

**Table 3**
Activation energy of the electrolyte conductivity before and after the melting point of SPEs obtained by the fitting of the Arrhenius plot and lithium transference number at 45 °C, 55 °C, 65 °C and 75 °C.

| Sample | Activation Energy ($E_a$) | | Transference number | | | |
|---|---|---|---|---|---|---|
| | *Before melting (kJ mol$^{-1}$)* | *After melting (kJ mol$^{-1}$)* | *45°C* | *55°C* | *65°C* | *75°C* |
| **Pristine** | 60.5 | 39.5 | 0.23 | 0.24 | 0.28 | 0.30 |
| **PEO-XG 5 %** | 47.4 | 33.3 | 0.24 | 0.25 | 0.31 | 0.32 |
| **PEO-XG 10 %** | 48.9 | 33.2 | 0.27 | 0.29 | 0.30 | 0.33 |
| **PEO-XG 20 %** | 50.6 | 32.7 | 0.26 | 0.27 | 0.33 | 0.38 |
| **PEO-XG 30 %** | 51.8 | 25.9 | 0.29 | 0.30 | 0.36 | 0.42 |

terminal hydroxyl groups along the PEO chain, which has been previously demonstrated to contribute in improved oxidative stability [71–73]. The stabilizing effect of XG becomes particularly evident when 20 % of the copolymer is incorporated, likely due to strengthened polymer-polymer interactions, leading to a more significant diminution of the free hydroxyl groups, as confirmed by DSC and FTIR analyses. Actually, the 20 % XG electrolyte demonstrated remarkable anodic stability, sustaining voltages up to approximately 4.9 V, as shown in Fig. 5c, and it was thus selected as the most promising electrolyte formulation.

XG 20 % anodic stability was further investigated in the potential range from 4 to 5 V by alternated LSV (100 mV increase at 0.1 mV s$^{-1}$ scan rate) and CA steps (1h duration at the upper voltage of the LSV steps), recording the resulting current during the latter, as shown in Fig. 5d. No significant current increases were recorded up to 4.8 V, which was set as the membrane oxidative limit. The electrochemical stability window measured for the most promising SPE formulation resulted to be significantly higher than the pristine, further confirming its suitability for future applications [74].

The cathodic stability of 20 % XG membrane was assessed via cyclic voltammetry within the 0.01–3 V range (Fig. 5c). During the first cycle, an irreversible peak below 1 V appeared, likely attributed to the formation of a passivation layer onto the working electrode surface, also known as SEI. However, in subsequent cycles, only reversible peaks associated with the carbon matrix of the WE are observed. The absence of degradation-related features confirms the stability of the membrane at low voltages, underscoring its possible compatibility with anodic materials.

### 3.5. Self-diffusion coefficients

The self-diffusion coefficients in the most promising membrane (20 % XG) were determined in the temperature range 303–333 K (below $T_m$), as illustrated by the $^7$Li NMR spectra in Fig. 6a. The measures were performed using PFG-NMR to directly determine the self-diffusion coefficients of both cations ($^7$Li) and anions ($^{19}$F). In all cases, the diffusion behavior was well described by Equation (1), as shown in Fig. 6b, indicating the presence of a single, well-defined self-diffusion coefficient at each temperature. The ionic diffusivities and the NMR-derived ionic conductivity ($\sigma_{NMR}$) are reported in Table S3. As expected, an increase in temperature resulted in a monotonic increase in both $D_{Li}^{+}$ and $D_{TFSI}^{-}$ (Fig. 6c), with the data exhibiting a linear trend consistent with the Arrhenius equation for diffusion (Equation (2)) [50,75]:

$$D = D_0 \cdot \exp(-E_D / RT), \quad (2)$$

where the slope of the dependence is determined by the activation energy for diffusion $E_D$. and $R$ is the universal gas constant. The diffusion coefficients obtained by NMR were subsequently compared with those calculated from electrochemical conductivity measurements ($\sigma_{EIS}$) over the same temperature range, using the Nernst–Einstein equation

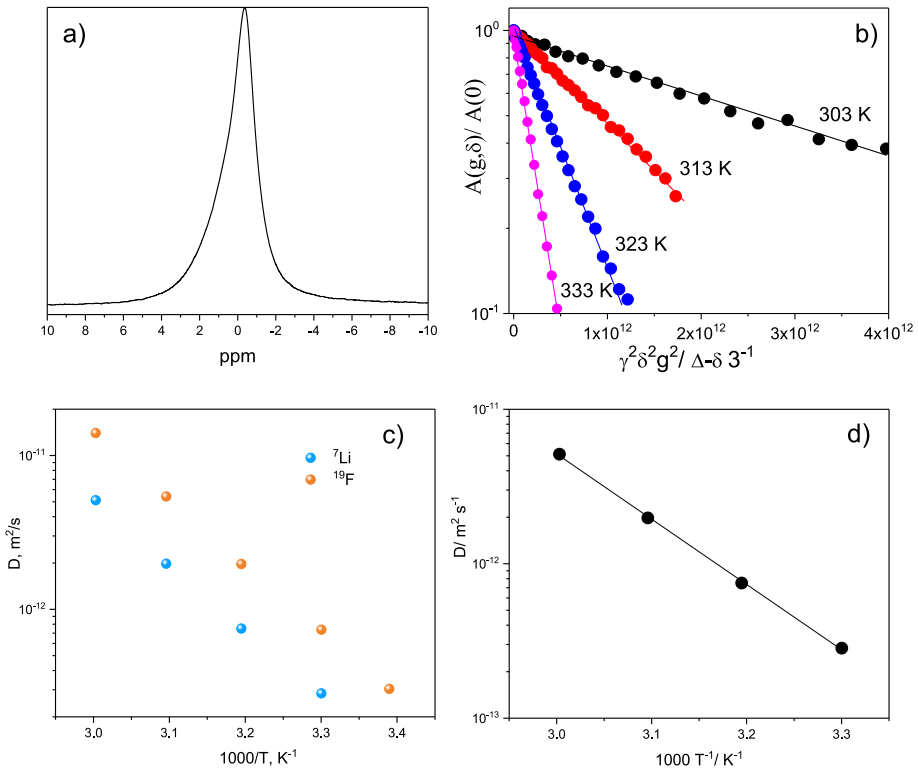



**Fig. 6.** (a) Typical $^{7}$Li NMR spectrum of 20 % XG membrane (T = 303 K). (b) $^{7}$Li diffusion decays obtained in the range 303–333 K. Arrhenius plot of temperature dependence for $Li^+$ and $TFSI^-$self-diffusion coefficients in the range 303–333 K calculated with (c) NMR and (d)diffusion coefficients calculated from electrochemical conductivity. Symbols correspond to experimental data, while the lines are the linear fits.

(Equation (3)) [75].

$$D = \frac{\sigma^* k_b^* T}{n^* q^2} \tag{3}$$

Where.

$\sigma$ = ionic conductivity (S $m^{-1}$)
$k_b$ = Boltzmann constant = 1.38 × $10^{-23}$ J $K^{-1}$
$T$ = absolute temperature (K)
$n$ = number density of charge carriers (1 $m^{-3}$)
$q$ = charge of the ion = 1.602 × $10^{-19}$ (C)

The $\sigma_{NMR}$ values are higher than the experimental conductivities measured by electrochemical impedance spectroscopy (Fig. 6d), probably due to the intrinsic differences of the two techniques. It should also be noted that $\sigma_{NMR}$ and $\sigma_{EIS}$ probe ionic motion at different scales: while PFG-NMR provides information on the self-diffusion of individual nuclei, reflecting local and short-range mobility, electrochemical impedance spectroscopy measures long-range, directional ion transport under an applied field [76,77]. Consequently, species that undergo local motion as part of neutral ion pairs or aggregates contribute to $\sigma_{NMR}$ but not to the macroscopic conductivity given by $\sigma_{EIS}$.

Consistently, the activation energy derived from the Arrhenius plot of the conductivity ($E_a$ = 50.6 kJ $mol^{-1}$) and from NMR ($E_D$ = 79 kJ $mol^{-1}$, Fig. S2) showed some discrepancy that may reflect the different physical processes probed by the two techniques: PFG-NMR characterizes short-range, thermally activated $Li^+$ hopping and desolvation from coordination sites, whereas electrochemical impedance measures net, field-driven charge transport across the sample. To quantify the effect of ion association on macroscopic transport, we define the association degree (α), which is well below unity over the measured temperature range. Particularly, α increases with temperature, indicating progressive ion pair/aggregate dissociation as the melting temperature is approached [78,79].

In both cases, the activation energy for diffusion is the energy required to overcome intermolecular interactions that act as energy barriers to molecular motion. However, in the case of conductivity technique, applied electric field contributes to the rupture of the part of the intermolecular contacts, while for the self-diffusion (PFG NMR) the system is in equilibrium (undisturbed by external forces), that takes more energy to break the intermolecular contacts.

### 3.6. Full-cell performances

The most promising solid polymer electrolyte formulation was further evaluated in a Li|XG 20 %|LFP full-cell configuration to assess membrane compatibility and long-term cycling stability. Specifically, commercial lithium iron phosphate was employed as the cathode material (XRD patterns provided in Fig. S3 in the SI for reference [80]), while metallic lithium served as anode. Fig. 7a shows the cycling performance of the cell cycled at 65 °C with a current density corresponding to C/10 (1C = 170 mA $g^{-1}$) within the 2.5–4.3 voltage window. After few activation cycles, the capacity stabilized at approximately 145 mAh $g^{-1}$ with nearly 100 % efficiency (Fig. 7b). The cell demonstrated excellent cycling performance with minimal capacity fading over 100 cycles, suggesting a good compatibility with the electrode materials. Additionally, the rate capability of the cell was assessed (Fig. S4) by applying progressively increasing current densities, ranging from C/10 to 1C, then restoring the initial lowest current density (where 1C = 170 mA $g^{-1}$). As before, the cell required a couple of activation cycles before reaching the optimal performance. Nevertheless, the specific capacity remains unaffected by an increase in current density from C/10 to C/5, with only a slight decrease observed at C/2, where it stabilizes around 130 mAh $g^{-1}$, accompanied by an improvement in coulombic efficiency. Even at 1C, the cell exhibited no signs of failure or dendrite formation, highlighting its exceptional stability across different operating

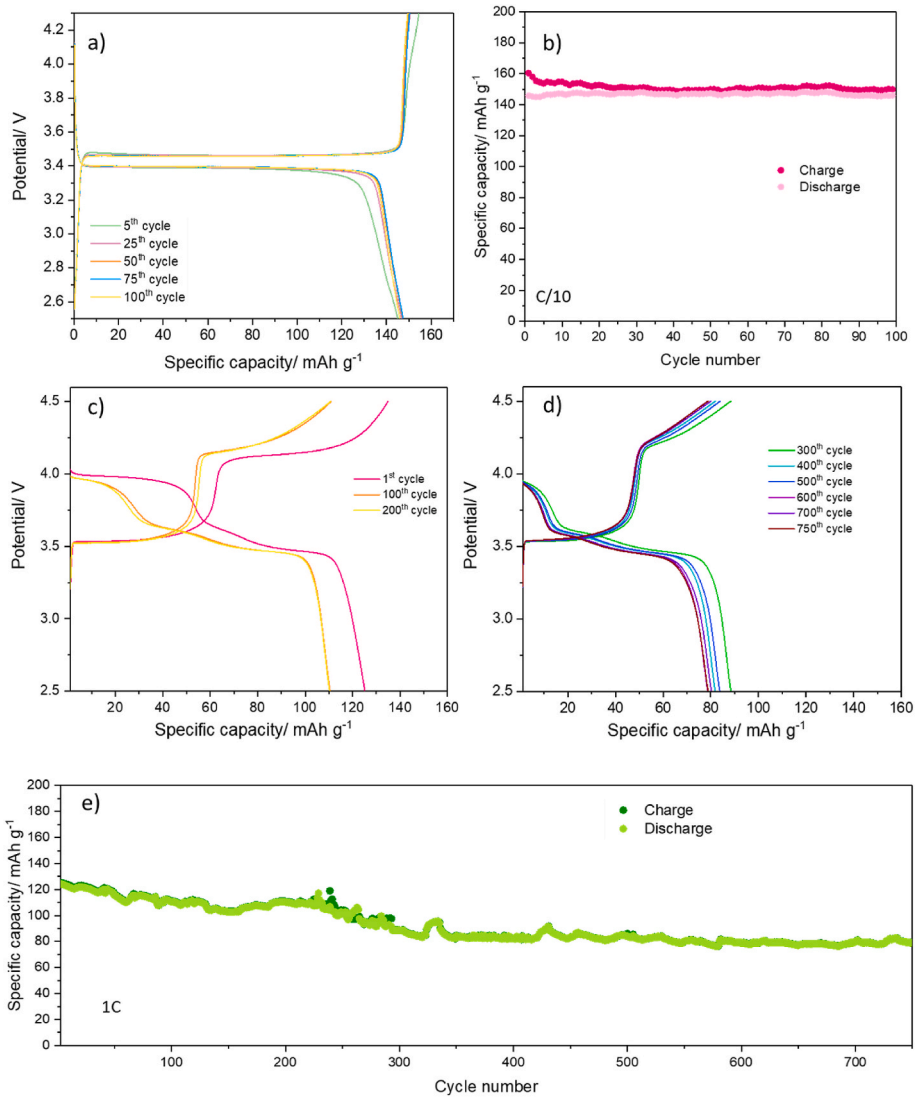



**Fig. 7.** (a) Cyclic performances of Li|20 %XG|LFP full cell cycled with a current density corresponding to C/10 (1C = 170 mA $g^{-1}$) within the 2.5–4.3 V voltage range along with (b) the corresponding cyclic trend. Galvanostatic profile of (c) the first 200 cycles and (d) up to 750 cycles of Li|20 %XG|LMFP cell in the 2.5–4.5 V voltage range with (e) corresponding cycling trend. All measurements were conducted at 65 °C.

conditions. When the current density was reverted to its initial values for 10 cycles, the capacity was fully restored, demonstrating the system excellent reversibility and long-term stability.

Building upon the promising results obtained with LFP, the XG 20 % membrane was further evaluated in a full cell configuration using a higher-voltage cathode: lithium manganese iron phosphate. The structural characteristics of LMFP are provided in the XRD pattern (shown in Fig. S5, see the SI**)**. To more rigorously assess the electrochemical stability of the membrane, the cell was operated over an extended voltage window up to 4.5 V (see voltage profile in Fig. 7c and d) and at a higher C-rate than the LFP-cathode cell. Following an activation phase consisting of three cycles at C/10, the cell was subsequently cycled at 1C. As shown in Fig. 7e, the system delivered a high specific capacity with an excellent capacity retention over time. Notably, the cell maintained stable performance for over 750 cycles, highlighting the remarkable electrochemical stability, durability and compatibility of the XG-based solid polymer electrolyte with higher-voltage cathodes.

## 4. Conclusions

In this study, 4 innovative solid polymer electrolytes were developed by blending polyethylene oxide with varying amounts of Xanthan gum. Comprehensive physicochemical and electrochemical characterization revealed an excellent performance in Li|SPE|Li symmetric cells, including high cycling stability and resistance to dendrite formation.

Among the investigated formulations, the solid polymer electrolyte incorporating 20 wt% XG exhibited the lowest overpotential, indicative of enhanced interfacial stability with lithium metal. Xanthan gum notably broadened the electrochemical stability window of the SPE, extending the anodic limit up to 4.8 V, as confirmed through linear sweep voltammetry. The 20 % XG electrolyte also demonstrated a high ionic conductivity and a reduced activation energy of 32.7 kJ $mol^{-1}$ post-melting, reflecting improved segmental motion within the polymer matrix. Additionally, the lithium-ion transference number reached 0.33 at the operating temperature, significantly higher than the value observed for the pristine PEO-based electrolyte (0.28), confirming improved ion transport selectivity and overall electrochemical performance.

The good compatibility and satisfactory cyclability with commercial $LiFePO_4$ cathodes further confirmed XG 20 % applicability in full cell configurations. When tested under more demanding conditions, such as those required by a higher-voltage LMFP cathode, delivering excellent cycling stability and minimal capacity fading over 750 cycles. These findings highlight the significant enhancement in both electrochemical

performance and interfacial stability imparted by XG incorporation, thereby establishing the PEO–XG blend polymer electrolyte as a compelling and sustainable candidate for advanced solid-state lithium-ion battery technologies.

## CRediT authorship contribution statement

**Asia Patriarchi:** Writing – review & editing, Writing – original draft, Methodology, Investigation, Formal analysis, Data curation, Conceptualization. **Hamideh Darjazi:** Methodology, Data curation. **Maddalena Barcaioni:** Methodology, Investigation. **Luca Minnetti:** Investigation, Data curation. **Alberto Fina:** Investigation, Formal analysis, Data curation. **Andrei Filippov:** Methodology, Investigation, Formal analysis, Data curation. **Faiz Ullah Shah:** Methodology, Investigation. **Oleg N. Antzutkin:** Methodology, Investigation, Data curation. **Miguel Ángel Muñoz-Márquez:** Writing – review & editing, Validation, Supervision, Methodology, Data curation, Conceptualization. **Francesco Nobili:** Writing – review & editing, Validation, Supervision, Funding acquisition, Conceptualization.

## Declaration of competing interest

The authors declare that they have no known competing financial interests or personal relationships that could have appeared to influence the work reported in this paper.

## Appendix A. Supplementary data

Supplementary data to this article can be found online at https://doi.org/10.1016/j.jpowsour.2025.238856.

## Data availability

Data will be made available on request.

## References


[1] I. Caldeira, et al., Ecologically friendly xanthan gum-PVA matrix for solid polymeric electrolytes, Ionics 24 (2018).
[2] Y. Guo, et al., Hydrogels and Hydrogel-Derived materials for energy and water sustainability, Chem. Rev. 120 (2020), https://doi.org/10.1021/acs.chemrev.0c00345. Preprint at.
[3] J.B. Goodenough, K.S. Park, The Li-ion rechargeable battery: a perspective, J. Am. Chem. Soc. 135 (2013), https://doi.org/10.1021/ja3091438. Preprint at.
[4] J.M. Tarascon, M. Armand, Issues and challenges facing rechargeable lithium batteries, Nature 414 (2001), https://doi.org/10.1038/35104644. Preprint at.
[5] A. Patriarchi, et al., Impact of prussian blue particle size distribution on electrochemical performance of gel polymer electrolyte-based Na-Ion cells, Chemelectrochem (2025), https://doi.org/10.1002/celc.202400350, 10.1002/celc.202400350.
[6] N. Nitta, F. Wu, J.T. Lee, G. Yushin, Li-ion battery materials: present and future, Mater. Today 18 (2015), https://doi.org/10.1016/j.mattod.2014.10.040. Preprint at.
[7] J. Aragane, et al., Development of 10 Wh class lithium secondary cells in the 'new sunshine program', J. Power Sources 68 (1997).
[8] S.P. Beaton, et al., On-road vehicle emissions: regulations, costs, and benefits, Science 268 (1995), https://doi.org/10.1126/science.268.5213.991. Preprint at.
[9] B. Scrosati, Challenge of portable power, Nature 373 (1995).
[10] B. Scrosati, J. Garche, Lithium batteries: status, prospects and future, J. Power Sources 195 (2010) 2419–2430, https://doi.org/10.1016/j.jpowsour.2009.11.048. Preprint at.
[11] J. Kalhoff, G.G. Eshetu, D. Bresser, S. Passerini, Safer electrolytes for lithium-ion batteries: state of the art and perspectives, ChemSusChem 8 (2015).
[12] Q. Wang, L. Jiang, Y. Yu, J. Sun, Progress of enhancing the safety of lithium ion battery from the electrolyte aspect, Nano Energy 55 (2019), https://doi.org/10.1016/j.nanoen.2018.10.035. Preprint at.
[13] L. Hu, S.S. Zhang, Z. Zhang, Electrolytes for Lithium and lithium-ion Batteries, 172, Green Energy and Technology, 2015.
[14] B. Song, et al., Dynamic Lithium distribution upon dendrite growth and shorting revealed by operando Neutron Imaging, ACS Energy Lett. (2019), https://doi.org/10.1021/acsenergylett.9b01652, 10.1021/acsenergylett.9b01652.
[15] X. Yang, J. Luo, X. Sun, Towards high-performance solid-state Li-S batteries: from fundamental understanding to engineering design, Chem. Soc. Rev. 49 (2020), https://doi.org/10.1039/c9cs00635d. Preprint at.
[16] Y. Zhou, et al., Four-armed branching and thermally integrated imidazolium-based polymerized ionic liquid as an all-solid-state polymer electrolyte for lithium metal battery, Electrochim. Acta 324 (2019).
[17] A. Manthiram, X. Yu, S. Wang, Lithium battery chemistries enabled by solid-state electrolytes, Nat. Rev. Mater. 2 (2017), https://doi.org/10.1038/natrevmats.2016.103. Preprint at.
[18] Q. Xiao, et al., Macroporous polymer electrolytes based on PVDF/PEO-b-PMMA block copolymer blends for rechargeable lithium ion battery, J Memb Sci 334 (2009).
[19] F. Wang, et al., Influence of additives in a PVDF-based solid polymer electrolyte on conductivity and Li-ion battery performance, Sustain. Energy Fuels 2 (2018).
[20] R. Miao, et al., PVDF-HFP-based porous polymer electrolyte membranes for lithium-ion batteries, J. Power Sources 184 (2008).
[21] M. Muthuvinayagam, C. Gopinathan, Characterization of proton conducting polymer blend electrolytes based on PVdF-PVA, Polymer (Guildf.) 68 (2015).
[22] Y.S. Zhu, et al., A new single-ion polymer electrolyte based on polyvinyl alcohol for lithium ion batteries, Electrochim. Acta 87 (2013).
[23] A. Hosseinioun, P. Nürnberg, M. Schönhoff, D. Diddens, E. Paillard, Improved lithium ion dynamics in crosslinked PMMA gel polymer electrolyte, RSC Adv. 9 (2019).
[24] E. Quartarone, P. Mustarelli, A. Magistris, PEO-based composite polymer electrolytes, Solid State Ion 110 (1998).
[25] A.C. Bloise, et al., Nuclear magnetic resonance study of PEO-based composite polymer electrolytes, Electrochim. Acta 46 (2001).
[26] D. Golodnitsky, G. Ardel, E. Peled, Ion-transport phenomena in concentrated PEO-based composite polymer electrolytes, Solid State Ion 147 (2002).
[27] G.B. Appetecchi, et al., Hot-pressed, dry, composite, PEO-based electrolyte membranes: I. Ionic conductivity characterization, J. Power Sources 114 (2003).
[28] J. Feng, et al., PEO based polymer-ceramic hybrid solid electrolytes: a review, Nano Convergence 8 (2021), https://doi.org/10.1186/s40580-020-00252-5. Preprint at.
[29] J. Ma, et al., A strategy to make high voltage LiCoO 2 compatible with polyethylene oxide electrolyte in all-solid-state lithium ion batteries, J. Electrochem. Soc. 164 (2017).
[30] Z. Lin, X. Guo, H. Yu, Amorphous modified silyl-terminated 3D polymer electrolyte for high-performance lithium metal battery, Nano Energy 41 (2017).
[31] D. Zhou, D. Shanmukaraj, A. Tkacheva, M. Armand, G. Wang, Polymer electrolytes for lithium-based batteries: advances and prospects, Chem 5 (2019), https://doi.org/10.1016/j.chempr.2019.05.009. Preprint at.
[32] A. Patriarchi, et al., All-Solid-State Li-Metal cell using nanocomposite TiO2/Polymer electrolyte and self-standing LiFePO4 cathode, Batteries 10 (2023) 11.
[33] F. Croce, G.B. Appetecchi, L. Persi, B. Scrosati, Nanocomposite polymer electrolytes for lithium batteries, Nature 394 (1998).
[34] F. Croce, L. Persi, F. Ronci, B. Scrosati, Nanocomposite polymer electrolytes and their impact on the lithium battery technology, Solid State Ion 135 (2000).
[35] R. DeWees, H. Wang, Synthesis and properties of NaSICON-type LATP and LAGP solid electrolytes, ChemSusChem 12 (2019), https://doi.org/10.1002/cssc.201900725. Preprint at.
[36] A. Patriarchi, et al., Evaluation of high-entropy (Cr, Mn, Fe, Co, ni)-oxide nanofibers and nanoparticles as passive fillers for solid composite electrolytes, Electrochim. Acta 512 (2025) 145425.
[37] S.A. Suthanthiraraj, M.K. Vadivel, Effect of propylene carbonate as a plasticizer on (PEO)50AgCF3SO3:SnO2 nanocomposite polymer electrolyte, Appl. Nanosci. 2 (2012) 239–246.
[38] K. Vignarooban, M.A.K.L. Dissanayake, I. Albinsson, B.E. Mellander, Effect of TiO2 nano-filler and EC plasticizer on electrical and thermal properties of poly(ethylene oxide) (PEO) based solid polymer electrolytes, Solid State Ion 266 (2014).
[39] M. Jakić, N.S. Vrandečić, I. Klarić, Thermal degradation of poly(vinyl chloride)/poly(ethylene oxide) blends: thermogravimetric analysis, Polym Degrad Stab 98 (2013).
[40] M. Basappa, et al., Preparation, characterization, and electrochemical properties of PEO/PVDF blend films, Chem. Phys. Lett. 799 (2022).
[41] N. Yazie, et al., Development of polymer blend electrolytes for battery systems: recent progress, challenges, and future outlook, Mater. Renew. Sustain. Energy (2023), https://doi.org/10.1007/s40243-023-00231-w. Preprint at.
[42] V. Bocharova, A.P. Sokolov, Perspectives for polymer electrolytes: a view from fundamentals of ionic conductivity, Macromolecules 53 (2020) 4141–4157, https://doi.org/10.1021/acs.macromol.9b02742. Preprint at.
[43] A.M. Regiani, et al., DSC and solid state NMR characterization of hydroxyethylcellulose/polyether films, Polym. Int. 49 (2000).
[44] S. Shanmuga Priya, M. Karthika, S. Selvasekarapandian, R. Manjuladevi, S. Monisha, Study of biopolymer I-carrageenan with magnesium perchlorate, Ionics 24 (2018).
[45] E. Raphael, C.O. Avellaneda, B. Manzolli, A. Pawlicka, Agar-based films for application as polymer electrolytes, Electrochim. Acta 55 (2010).
[46] A. Pawlicka, et al., Dielectric behavior and FTIR studies of xanthan gum-based solid polymer electrolytes, Electrochim. Acta 305 (2019).
[47] F.C. Tavares, D.S. Dörr, A. Pawlicka, C. Oropesa Avellaneda, Microbial origin xanthan gum-based solid polymer electrolytes, J. Appl. Polym. Sci. 135 (2018).
[48] P. Saranya, D. Vanitha, K. Sundaramahalingam, M. Nandhinilakshmi, S.A. Samad, Structural and electrical properties of cross-linked blends of Xanthan gum and polyvinylpyrrolidone-based solid polymer electrolyte, Ionics 29 (2023).
[49] J. Evans, C.A. Vincent, P.G. Bruce, Electrochemical measurement of transference numbers in polymer electrolytes, Polymer (Guildf.) 28 (1987).
[50] H. Pfeifer, Principles of nuclear magnetic resonance microscopy, Zeitschrift für Physikalische Chemie 176 (1992).

[51] S.A.M. Noor, A. Ahmad, I.A. Talib, M.Y.A. Rahman, Morphology, chemical interaction, and conductivity of a PEO-ENR50 based on solid polymer electrolyte, Ionics 16 (2010).
[52] L. Pham, et al., A dual synergistic of curcumin and gelatin on thermal-responsive hydrogel based on Chitosan-P123 in wound healing application, Biomed. Pharmacother. 117 (2019).
[53] K. Zhu, Y. Liu, J. Liu, A fast charging/discharging all-solid-state lithium ion battery based on PEO-MIL-53(Al)-LiTFSI thin film electrolyte, RSC Adv. 4 (2014).
[54] S. Faria, et al., Characterization of xanthan gum produced from sugar cane broth, Carbohydr. Polym. 86 (2011).
[55] V.J. Bulbul, P.R. Bhushette, R.S. Zambare, R.R. Deshmukh, U.S. Annapure, Effect of cold plasma treatment on Xanthan gum properties, Polym. Test. 79 (2019).
[56] A.J. Kora, R.B. Sashidhar, J. Arunachalam, Gum kondagogu (cochlospermum gossypium): a template for the green synthesis and stabilization of silver nanoparticles with antibacterial application, Carbohydr. Polym. 82 (2010).
[57] P. De Sainte Claire, Degradation of PEO in the solid state: a theoretical kinetic model, Macromolecules 42 (2009).
[58] A. Patriarchi, et al., Unlocking sustainable-by-design li-metal batteries by recycled PVB in blend polymer electrolytes, ChemSusChem (2025) 2501288.
[59] J. Patel, B. Maji, N.S.H.N. Moorthy, S. Maiti, Xanthan gum derivatives: review of synthesis, properties and diverse applications, RSC Adv. 10 (2020), https://doi.org/10.1039/d0ra04366d. Preprint at.
[60] Y. Tao, et al., Rheological behavior and microstructure of release-controlled hydrogels based on xanthan gum crosslinked with sodium trimetaphosphate, Food Hydrocoll. 52 (2016).
[61] V. Marangon, Y. Tominaga, J. Hassoun, An alternative composite polymer electrolyte for high performances lithium battery, J. Power Sources 449 (2020).
[62] P. Yao, et al., Review on polymer-based composite electrolytes for lithium batteries, Front. Chem. 7 (2019), https://doi.org/10.3389/fchem.2019.00522. Preprint at.
[63] F. Croce, et al., Physical and chemical properties of nanocomposite polymer electrolytes, J. Phys. Chem. B 103 (1999).
[64] J.L. Olmedo-Martínez, et al., All-Polymer nanocomposite as salt-free solid electrolyte for lithium metal batteries, ACS Polymers Au 4 (2024).
[65] B.A.A. Boukamp, Nonlinear least squares Fit procedure for analysis of immittance data of electrochemical systems, Solid State Ion 20 (1986).
[66] B.A. Boukamp, A package for impedance/admittance data analysis, Solid State Ion (1986) 18–19.
[67] K.J. Laidler, The development of the arrhenius equation, J Chem Educ 61 (1984).
[68] K.M. Diederichsen, H.G. Buss, B.D. McCloskey, The compensation effect in the vogel-tammann-fulcher (VTF) equation for polymer-based electrolytes, Macromolecules 50 (2017).
[69] A.B. Puthirath, et al., Transparent flexible lithium ion conducting solid polymer electrolyte, J Mater Chem A Mater 5 (2017).
[70] J. Fu, Z. Li, X. Zhou, X. Guo, Ion transport in composite polymer electrolytes, Mater. Adv. 3 (2022), https://doi.org/10.1039/d2ma00215a. Preprint at.
[71] S. Wu, et al., In-situ preparation of gel polymer electrolyte with glass fiber membrane for lithium batteries, J. Power Sources 472 (2020).
[72] Z. Hei, S. Wu, H. Zheng, H. Liu, H. Duan, Increasing the electrochemical stability window for polyethylene-oxide-based solid polymer electrolytes by understanding the affecting factors, Solid State Ion 375 (2022).
[73] X. Yang, et al., Determining the limiting factor of the electrochemical stability window for PEO-based solid polymer electrolytes: main chain or terminal -OH group? Energy Environ. Sci. 13 (2020).
[74] J. Qiu, et al., Enabling stable cycling of 4.2 V high-voltage all-solid-state batteries with PEO-Based solid electrolyte, Adv. Funct. Mater. 30 (2020).
[75] P. Atkins, J. de Paula, J. Keeler, Atkins' Physical Chemistry. Atkins', Phys. Chem. (2022) https://doi.org/10.1093/hesc/9780198847816.001.0001.
[76] E. Quartarone, et al., Ions dynamics and diffusion in self-healing chemical gel electrolytes for Li-ion batteries, Chemelectrochem 10 (2023).
[77] D.J. Morales, S. Greenbaum, NMR investigations of crystalline and glassy solid electrolytes for lithium batteries: a brief review, Int. J. Mol. Sci. 21 (2020).
[78] L. Carbone, et al., Relevant features of a triethylene glycol Dimethyl ether-based electrolyte for application in lithium battery, ACS Appl. Mater. Interfaces 9 (2017).
[79] R. Poiana, et al., Safe gel polymer electrolytes for high voltage Li-batteries, Electrochim. Acta 401 (2022).
[80] L. Minnetti, et al., New design high energy density Li-ion battery based on self-standing electrodes configuration, Electrochim. Acta 536 (2025).